Contrasting relationship between wintertime blocking highs over Europe-Siberia and temperature anomalies in the Yangtze River basin

Ning Shi*

Collaborative Innovation Center on Forecast and Evaluation of Meteorological Disasters, Key Laboratory of Meteorological Disaster of Ministry of Education, Nanjing University of Information Science and Technology, Nanjing, China.

SuolangTajie, Pinyu Tian, Yicheng Wang

College of Atmospheric Science, Nanjing University of Information Science and Technology, Nanjing, China.

Xiaoqiong Wang

Shanxi Climate Center, Taiyuan, China.

Corresponding author:
Dr. Ning Shi, Nanjing University of Information Science and Technology, Nanjing 210044, China. E-mail: shining@nuist.edu.cn

Early Online Release: This preliminary version has been accepted for publication in *Monthly Weather Review*, may be fully cited, and has been assigned DOI 10.1175/MWR-D-19-0152.1. The final typeset copyedited article will replace the EOR at the above DOI when it is published.

Abstract

Based on the Japanese 55-year reanalysis dataset, this study identifies 92 Europe-Siberia blocking high events (ESBs) over the 60 winters (November to March) from 1958/1959 to 2017/2018. According to the influence on the surface air temperature at 2 m over the middle and lower reaches of the Yangtze River, the ESBs are classified into three types: cold, neutral and warm. Although cold-type ESBs are dominant, the number of warm-type ESBs is not negligible. The present study mainly focuses on the differences between cold-type and warm-type ESBs.

Both the cold-type ESBs and the warm-type ESBs are characterized by height anomalies with a northwest-southeast tilting dipole pattern over the Eurasian continent in the mid- and upper troposphere. However, the tilting dipole pattern of the warm type is located to the northwest of its cold-type counterpart, which reflects differences in the propagation of Rossby wave packets. The Siberian high is stronger in cold-type ESBs than in warm-type ESBs. The induced advection of the climatological mean air temperature by the anomalous meridional wind velocity in the lower troposphere accounts for the largest portion of the observed tendency of the air temperature for both ESB types. In addition, diabatic heating tends to counteract the local cooling tendency of air temperature over the Yangtze River region for the cold-type ESBs. Finally, cold-type ESBs are generally characterized by air parcels originating in the region to the north and northeast of the Tibetan Plateau, while warm-type ESBs are characterized by diverse trajectories.

Accepted for publication in *Monthly Weather Review*. DOI 10.1175/MWR-D-19-0152.1.

Keywords: blocking high, surface air temperature, Rossby wave propagation, Siberian high

1 Introduction

A blocking high is a large-scale anomalous atmospheric phenomenon that occurs over middle and high latitudes. Because blocking highs are highly persistent (e.g., Knox and Hay 1984), they can cause extreme weather in the areas they directly or indirectly affect. Moreover, due to the complexity of their formation and maintenance, blocking highs pose a challenge for medium-range weather forecasts (Matsueda and Palmer 2018). Blocking highs can be detected throughout the year, but they are more persistent and more intense in the cold season (e.g., Tibaldi et al. 1994; Lupo and Smith 1995; Barriopedro et al. 2006).

Climatologically, in boreal winter, blocking highs tend to occur over the Euro-Atlantic region and the central and eastern Pacific (e.g., Dole and Gordon 1983; Tibaldi and Molteni 1990; Pelly and Hoskins 2003; Schwierz et al. 2004; Barriopedro et al. 2006). In addition, the frequency of blocking highs is also high around the Ural Mountains, which is usually considered the third most preferential region for the occurrence of blocking highs (Dole and Gordon 1983; Lupo and Smith 1995; Wiedenmann et al. 2002). In particular, blocking highs around the Ural Mountains have been regarded as important upstream precursors of severe cold surges in East Asia (Tao 1957; Takaya and Nakamura 2005b; Cheung et al. 2013). For example, the

Accepted for publication in *Monthly Weather Review*. DOI 10.1175/MWR-D-19-0152.1.

blocking frequency in the Ural Mountains in January 2008 exceeded the 95th percentile for the period 1950–2007 (Zhou et al. 2009), and the blocking highs were regarded as an important circulation contributor to the long-lasting and severe snow and freezing rain that affected southern China (Tao and Wei 2008; Wen et al. 2009; Bueh et al. 2011a). Thus, exploring the dynamical processes of blocking highs around the Ural Mountains can improve our understanding of the variability of the surface air temperature (SAT) anomalies over East Asia.

Cheung et al. (2013) showed the climatological aspects and evolutionary features of the Ural-Siberia blocking high in boreal winter via thermodynamic and geostrophic vorticity tendency equations. They noted that the horizontal advections of both vorticity and air temperature played fundamental roles in the generation of Ural-Siberia blocking highs. In their study, a Ural-Siberia blocking high refers to a blocking high centered in the interval [30°–100°E], which covers parts of Europe and the Ural Mountains. Based on winter-mean data, Cheung et al. (2012) implied that the 30°–100°E region is so broad that it can obscure the seasonal influences over East Asia of the blocking highs over the Ural Mountains and over Eastern Europe. Moreover, Luo et al. (2016b) noted that blocking highs over different regions around the Ural Mountains can exert different influences on the temperature anomalies over Eurasia. Figure 7 in their paper illustrates that the Ural blocking highs are accompanied by 11-day mean SAT anomalies extending from midlatitude Eurasia southeastward to eastern China. Note that the 11-day mean SAT anomaly in Luo et al.

Accepted for publication in *Monthly Weather Review*. DOI 10.1175/MWR-D-19-0152.1.

(2016b) is averaged from 5 days preceding to 5 days after the peak day of the Ural blocking high. However, for eastern China or East Asia, the strongest cold anomalies generally occur over the decay stage of Ural blocking highs (Tao 1957; Takaya and Nakamura 2005b; Cheung et al. 2013). Moreover, cold surges originating from mid- and high latitudes over Asia usually propagate southeastward along the northeastern slope of the Tibetan Plateau and can reach as far south as the middle and lower reaches of the Yangtze River or even the South China Sea (Tao 1957; Ding and Krishnamurti 1987). Therefore, exploring whether differences exist in the SAT anomalies over eastern China after the peak days of the blocking highs over the Ural-Siberia region, which constitutes the main issue of the present study, is a worthwhile endeavor.

For an improved understanding in this regard, the different underlying dynamical features of the different types of blocking highs should be identified. Many previous studies have shown that upstream quasi-stationary Rossby wave packets can facilitate the formation of persistent anticyclone anomalies (Nakamura 1994; Nakamura et al. 1997; Takaya and Nakamura, 2005a; Cheung et al. 2013; Luo et al. 2016b). The present study will discuss, among other things, the differences in the propagation of the Rossby wave packets during the formation of different types of blocking highs over the Ural-Siberia region.

Furthermore, many studies have shown that teleconnection patterns (Horel, 1981; Wallace and Gutzler, 1981; Barnston and Livezey, 1987) are evident in both the

Accepted for publication in *Monthly Weather Review*. DOI 10.1175/MWR-D-19-0152.1.

evolution of blocking highs over the Eurasian continent and the SAT anomalies over East Asia. Luo et al. (2016b) showed that the number of Ural blocking highs that are preceded by a positive North Atlantic Oscillation accounts for nearly 60% of all Ural blocking highs. In addition, the Scandinavian pattern, another important wintertime teleconnection pattern, generally precedes the formation of blocking highs over Europe (Tyrlis and Hoskins, 2008). The Scandinavian pattern also emerged as a precursory circulation pattern for the extremely persistent cold weather over southern China in January 2008 (Bueh et al. 2011a; Zhou et al. 2009). Takaya and Nakamura (2005b) pointed out that there are two origins of the amplification of the Siberian high, i.e., the “Atlantic origin” and the “Pacific origin”. The “Atlantic origin” might be associated with the Eurasian pattern (Wang and Zhang, 2014), while the “Pacific origin” might be associated with the West Pacific pattern. Although these studies hint that blocking highs are associated with teleconnection patterns, a significance test for their relationships is lacking. Thus, the present study discusses the relationship between the blocking highs and several teleconnection patterns that have primary anomaly centers over or around the Eurasian continent.

To explore the abovementioned issues, the remainder of this paper is organized as follows: Section 2 introduces the data and methods employed to detect the blocking highs around the Ural Mountains and diagnose their dynamical features; Section 3 describes the method used to classify those blocking highs and shows some statistical results; Section 4 presents a comparison between the different evolution and

Accepted for publication in *Monthly Weather Review*. DOI 10.1175/MWR-D-19-0152.1.

mechanisms of the two types of blocking highs, while Section 5 provides the main conclusions of this study and further discussion.

2 Data and Methods

2.1 Data

The 6-hourly fields from the Japanese 55-year reanalysis (JRA-55) project conducted by the Japan Meteorological Agency from 1958 to 2018 (Kobayashi et al. 2015) are mainly analyzed in this study. Daily mean fields are obtained from these 6-hourly fields. This study limits the analysis to 60 years of the extended boreal winter period, i.e., from November to March of the following year. The horizontal resolution of this dataset is 1.25°×1.25°.

This study uses meteorological variables on isobaric surfaces, including the geopotential height, wind velocity, and air temperature. To measure the influence of different types of blocking highs on the surface weather, the SAT, sea level pressure (SLP) and surface pressure are also utilized. The monthly geopotential height at 500 hPa (Z500) is also used to obtain the teleconnection patterns. All of the abovementioned variables are reanalysis fields based on the assimilation of observational data. In addition, the surface geopotential is used to represent large orographic features.

The diabatic heating rate at 950 hPa is also used to identify the formation of near-surface air temperature anomalies over the Yangtze River region. In JRA-55, the

Accepted for publication in *Monthly Weather Review*. DOI 10.1175/MWR-D-19-0152.1.

diabatic heating rate is composed of the large-scale condensation heating rate, convective heating rate, vertical diffusion heating rate, solar radiative heating rate and longwave radiative heating rate. The large-scale condensation heating rate represent the heating effect by large-scale forced uplift, while the convective heating rate represent the heating effect by cumulus convection. The vertical diffusion heating rate represents the contribution from the turbulent transport of heat in the planetary boundary layer. The longwave radiative heating rate and the solar heating rate are the two diabatic heating fields associated with radiation. In contrast to the abovementioned reanalysis fields, the five diabatic heating fields are diagnostic fields. The parameterization methods for deriving the five diabatic heating rates are described by Kobayashi et al. (2015), and more details can be found in an online document (https://www.jma.go.jp/jma/jma-eng/jma-center/nwp/outline2013-nwp/index.htm).

2.2 Methods

2.2.1 Data Processing

The methods utilized to obtain the anomaly field are the same as those employed in Nakamura et al. (1997). The local anomaly of a given variable on a particular day is defined as its departure from the local value of the climatological mean annual cycle for the corresponding calendar date. The climatological mean annual cycle is defined as the 31-day running mean of the 60-year climatological mean daily fields. The

Accepted for publication in *Monthly Weather Review*. DOI 10.1175/MWR-D-19-0152.1.

purpose of applying the 31-day running mean to the 60-year climatological mean daily fields is to further minimize the day-to-day variability.

2.2.2 Definition of Blocking High

The blocking identification method of Tibaldi and Molteni (1990) is used to detect blocking highs around the Ural Mountains. First, the instantaneous local blocking index is calculated at every longitude,

$$\begin{cases} \text{GHGN}=\dfrac{Z(\phi_n)-Z(\phi_0)}{\phi_n-\phi_0} \\ \\ \text{GHGS}=\dfrac{Z(\phi_0)-Z(\phi_s)}{\phi_0-\phi_s} \end{cases} \tag{1}$$

where Z is the daily geopotential height at 500 hPa, GHGN refers to the meridional gradients to the north of a chosen reference latitude ϕ_0, while GHGS refers to the meridional gradients to the south. Here, ϕ_n=80°N+Δ, ϕ_0=60°N+Δ, and ϕ_s=40°N+Δ, where Δ is a variable whose value is set from -5° to +5° with an interval of 1.25° instead of Δ=0°,$\pm$4° in the original index because the JRA data has a horizontal resolution of 1.25°. An instantaneous local blocking is considered to occur if GHGN$<$ -10 m/degree and GHGS$>$0 for at least one value of Δ. Then, a blocking high event is considered to occur around the Ural Mountains if the instantaneous local blocking occurs over at least 15 consecutive degrees longitude within the longitudinal sector from 30°E to 100°E and persists for at least 4 days. The region from 30°E to 100°E is approximately centered on the longitude (60°E) of the Ural Mountains. The

Accepted for publication in *Monthly Weather Review*. DOI 10.1175/MWR-D-19-0152.1.

longitudinal sector with consecutive blocking occurrence is referred to as the blocking region in which the primary anticyclonic anomaly center is searched.

As proposed by Barriopedro et al. (2010), a blocking high flow is characterized not only by a gradient-reversed configuration, which is the basic idea for defining a blocking flow in Tibaldi and Molteni (1990) and Pelly and Hoskins (2003), but also by persistent height anomalies (Dole and Gordon 1983). Accordingly, we include an additional constraint requiring the amplitude of the geopotential height anomaly at 500 hPa at the primary anomaly center to exceed 5 gpdm. For a particular blocking high event on a particular day, the location of the primary anomaly center is identified as the grid point with the maximum height anomaly within the blocking region bounded by 55°N and 80°N. Accordingly, all of these blocking highs are referred to as Europe-Siberia blocking highs (ESBs). We choose to define the ESB peak day as the day with the largest anomaly height in the primary anomaly center. In sections 3 and 4, the peak day is regarded as the reference day for the composite analysis. Moreover, day 0 refers to the peak day, and day N (-N) refers to N days after (before) the peak day.

2.2.3 Significance Test

The statistical significance of the ESB composite anomalies is tested based on two-tailed Student's *t* tests at each grid point. As noted by Wilks (2016), the false discovery rate (FDR) should be controlled in multiple hypothesis tests in the case of over-optimistic significance results. Following Wilks (2016), the threshold value for

Accepted for publication in *Monthly Weather Review*. DOI 10.1175/MWR-D-19-0152.1.

the significance level, p^*_{FDR}, is determined based on the distribution of ascending sorted p values:

$$p^*_{\mathrm{FDR}} = \max_{i=1,\dots,N}[p_{(i)} \le (i/N)\alpha_{\mathrm{FDR}}] \quad (2)$$

where $p_{(i)}$ is the i-th smallest p value of all p values evaluated at each grid point of a composite map, N is the total number of grid points, and the control level for the FDR, α_{FDR}, is set to 0.05 throughout our study. After applying the FDR procedure, the proportion of falsely rejected null hypotheses is effectively controlled. In the following, the p^*_{FDR} value is indicated in the relevant figure captions.

2.2.4 Thermodynamic Energy Equation at the Lower Troposphere

The thermodynamic energy equation (Holton 2004, their equation 2.42) is employed to diagnose the formation of air temperature anomalies in the lower troposphere over the Yangtze River region. Every term can be represented as the sum of its local anomaly and the climatological mean. After removing the terms describing the climatological mean state, Eq. (3) gives the tendency equation for the anomalous air temperature *T*':

$$\underset{\text{obs}}{\frac{\partial T'}{\partial t}} = \underbrace{-\left(u\frac{\partial T}{\partial x}\right)'}_{\text{x\_adv}} \underbrace{-\left(v\frac{\partial T}{\partial x}\right)'}_{\text{y\_adv}} \underbrace{-\left(\omega\frac{\partial T}{\partial p}\right)' + \frac{R}{C_p p}(T\omega)'}_{\text{z\_mot}} + \underset{\text{dia}}{\frac{Q'}{C_p}} \quad (3)$$

where prime indicates the local anomaly. The terms u, v, and ω represent the velocity on isobaric surfaces. The units of u and v are m/s, and the unit of ω is Pa/s. C_p is the specific heat at constant pressure, R is the gas constant of dry air, and Q is the rate of

Accepted for publication in *Monthly Weather Review*. DOI 10.1175/MWR-D-19-0152.1.

diabatic heating per unit mass. The terms of Eq. (3) from left to right represent (I) the observed tendency of the air temperature anomaly, (Ⅱ) the advection in the zonal direction and (Ⅲ) that in the meridional direction, (Ⅳ) the contribution from the vertical motions and (Ⅴ) the diabatic heating; these terms are denoted obs, x_adv, y_adv, z_mot, and dia, respectively, in the corresponding analyses in Section 4.2. Note that the 6-hourly fields are used to evaluate each term in Eq. (3). To be consistent with the analysis in Sections 4.1 and 4.4, which are based on daily mean fields, the obtained 6-hourly terms in Eq. (3) are finally daily averaged.

Note that the discretized thermodynamic equation of Eq. (3) is not closed due to various errors in the budget analysis (including temporal and spatial discretization errors, imperfect descriptions of both the real state of the atmosphere and the real diabatic heating fields by the JRA-55 datasets, etc.). To evaluate the uncertainty of our analysis due to the errors, the residual term is also calculated as the difference between the “obs” term on the left-hand side of Eq. (3) and the sum of the four terms on the right-hand side of Eq. (3). Thus, the residual term includes the sum of the various errors. In Section 4.2, the potential influences of the errors are discussed.

2.2.5 Trajectory Analysis

The backward trajectories of air parcels in the lower troposphere over the Yangtze River region are analyzed with the tool developed by Wernli and Davies (1997). The method can be expressed using the following equation:

Accepted for publication in *Monthly Weather Review*. DOI 10.1175/MWR-D-19-0152.1.

$$\begin{cases} r^{*n-1} = r^n - U(r^n)\Delta t \\ U^* = [U(r^n) + U(r^{*n-1})]/2 \end{cases} \quad (4)$$

where r^n represents the three-dimensional location vector of an air parcel at the *n-th* timestep, r^{*n-1} represents the potential location vector at the previous timestep, U represents the three-dimensional wind velocity at the regular longitude/latitude grids, and U^* represents the adjusted mean wind. The wind velocity at a particular grid between the regular grids, which is denoted by $U(r^{*n-1})$, is obtained by bilinear interpolation in both the horizontal and vertical directions. The 6-hourly fields are used to calculate the trajectories of air parcels, and Δt is accordingly set to 21600 s. The location vector at the *(n-1)-th* timestep is finally obtained by 100 iterations performed on Eq. (4). The backward tracing is terminated if the air parcel is found to exist underground, which is determined when the value of the pressure surface at which the air parcel is located is larger than the local surface pressure.

Following the method of Zschenderlein et al. (2018), we also analyze the evolution of the temperature and the potential temperature of a particular air parcel along its trajectory. If the potential temperature varies slightly while the temperature varies considerably, the adiabatic process is inferred to be dominant during the movement of the air parcel. In contrast, the diabatic process is inferred to dominate if the potential temperature varies greatly.

2.2.6 Wave-Activity Flux

Accepted for publication in *Monthly Weather Review*. DOI 10.1175/MWR-D-19-0152.1.

The wave-activity flux formulation derived by Takaya and Nakamura (1997, 2001) is used. The flux is independent of the wave phase without any temporal or zonal averaging and is parallel to the local group velocity of stationary Rossby wave packets in the Wentzel–Kramers–Brillouin sense. Thus, this flux is suitable for diagnosing the propagation of the low-frequency Rossby wave packets associated with ESBs on a zonally varying basic flow. The flux on the isobaric surface is expressed as follows:

$$W = \frac{p}{2000|\boldsymbol{U}|}\left(\begin{array}{l} \left[u\left(v'^2 - \psi' v'_x\right) + v\left(-u'v' + \psi' u'_x\right)\right]\ \vec{i} + \\ \left[u\left(-u'v' + \psi' u'_x\right) + v\left(u'^2 + \psi' u'_y\right)\right]\ \vec{j} + \\ \left\{\dfrac{f_0 R_a}{N^2 H_0}\left[u\left(v'T' - \psi' T'_x\right) + v\left(-u'T' - \psi' T'_y\right)\right]\right\}\vec{k} \end{array}\right) \tag{5}$$

where the prime symbol denotes a low-frequency perturbation and $\boldsymbol{U} = (u, v)$ is the horizontal basic flow velocity. The low-frequency circulation is obtained by applying the Lanczos filter (Duchon 1979) with a cut-off frequency of 8 days. In this study, the low-frequency perturbations in Eq. (5) are obtained by the composites of the daily low-frequency anomalies associated with ESBs, while the basic flow $\boldsymbol{U}$ is represented by the climatological mean annual cycle, which has been described in Section 2.2.1. The subscripts indicate partial differentiation, whereas the other notations in Eq. (5) are standard.

2.2.7 Teleconnection Pattern Indices

Accepted for publication in *Monthly Weather Review*. DOI 10.1175/MWR-D-19-0152.1.

The teleconnection patterns are first obtained through rotated principal component analysis as in Barnston and Livezey (1987) but with minor modifications. A brief description is provided here. First, the ten leading unrotated empirical orthogonal functions are determined from the standardized monthly Z500 height anomalies in the 20-90°N region with a temporal sequence of 60 years×5 months/year =300 months. Then, the ten leading rotated modes are obtained by applying the Kaiser varimax rotation to the ten unrotated modes. Excluding a spurious mode that has not been documented by previous studies and seems to have no apparent physical meaning, nine evident teleconnection patterns are recognized: North Atlantic Oscillation, polar/Eurasia (or Northern Asia pattern in Barnston and Livezey (1987)), West Pacific, Pacific/North American, East Atlantic/West Russia, East Atlantic, tropical/Northern Hemisphere, East Pacific–North Pacific and Scandinavian patterns. The Scandinavian pattern was referred to as the Eurasia-1 pattern, and the East Atlantic/West Russia pattern was referred to as the Eurasia-2 pattern by Barnston and Livezey (1987). The present study will mainly discuss the following six patterns, North Atlantic Oscillation, polar/Eurasia, West Pacific, East Atlantic/West Russia, East Atlantic and Scandinavian patterns, all of which have their primary centers of action around the Eurasian continent.

The daily indices of the six teleconnection patterns are obtained by projecting the standardized daily Z500 anomalies to the teleconnection patterns, which is similar to the method used by Baldwin and Dunkerton (2001) to calculate the daily Arctic

Accepted for publication in *Monthly Weather Review*. DOI 10.1175/MWR-D-19-0152.1.

Oscillation index (although the nonstandardized anomalies are utilized there). The daily index for each of the six teleconnection patterns is further normalized locally by its standard deviation over 31 days/year×60 years =1860 days, where the annual 31-day sequence is centered on that calendar day.

3 Classification of ESBs

According to the detection method described in Section 2.2.2, 92 ESBs are detected during the 60 boreal winters. The 7-day averaged composite results of the 92 ESBs are shown in Figure 1. The height anomalies at 500 hPa are averaged from day -3 to day 3 (Figure 1a). Significant anticyclonic height anomalies occur over northwestern Eurasia with a primary center at approximately [55°E, 65°N], while significant cyclonic height anomalies are mainly located to the southeast and southwest of the anticyclonic height anomalies. This spatial pattern is similar to that of the Ural-Siberia blocking highs on the peak day in Cheung et al. (2013). To show the influence of ESBs on the SAT during their decay stage, the composite SAT anomalies (Figure 1b) are averaged from day 1 to day 7. Warm SAT anomalies occur over the polar region, while cold anomalies occur over the middle latitudes of Eurasia; this phenomenon is sometimes referred to as the "warm Arctic–cold continent (Eurasia)" pattern (Overland et al. 2011; Luo et al. 2016a). This temperature pattern describes the out-of-phase relationship between the SAT anomalies over the Arctic and those over the midlatitude Eurasian continent. Significant midlatitude negative

Accepted for publication in *Monthly Weather Review*. DOI 10.1175/MWR-D-19-0152.1.

SAT anomalies also extend southeastward along the northeastern slope of the Tibetan Plateau, reaching as far as the Yangtze River region ([106.25–118.75°E, 25–32.5°N], green rectangle in Figure 1b). Therefore, the overall relationships between the upstream blocking highs and the SAT over the Yangtze River region are basically consistent with those observed in previous studies (Tao 1957; Takaya and Nakamura 2005b; Cheung et al. 2013).

To further explore the subsequent influence of ESBs, Figure 2 shows the SAT anomalies averaged over the area of the Yangtze River after the peak days of the 92 ESBs. Evidently, many ESBs are followed by negative SAT anomalies, which is consistent with both the results of early studies on ESBs (Tao 1957; Takaya and Nakamura 2005b) and the results shown in Figure 1. However, for some of the ESBs, the Yangtze River region is dominated by positive SAT anomalies. This phenomenon inspires us to classify the ESBs according to the mean values of the SAT anomalies over the Yangtze River region after the peak days of the ESBs.

Here, the area-averaged SAT anomalies are averaged from day 3 to day 4, during which the SAT anomalies display a relatively large spread. An ESB event is regarded as a warm type if the 2-day mean SAT anomaly is higher than 1°C or a cold type if the 2-day mean SAT anomaly is lower than -1°C. The remaining ESBs are regarded as the neutral type. Finally, the 92 ESBs are classified into 54 cold-type events, 14 neutral-type events and 24 warm-type events. Clearly, the cold type is dominant, but the number of warm-type events is not negligible, accounting for approximately 26%

Accepted for publication in *Monthly Weather Review*. DOI 10.1175/MWR-D-19-0152.1.

of all ESBs. The difference in the composite SAT anomalies between the two types of ESBs (shown by the thick lines in Figure 2) is most evident from day 3 to day 4, which is consistent with our choice of this particular 2-day period to classify the ESBs.

With regard to the ESBs of the same type, evident case-to-case variability occurs in the SAT anomalies over the Yangtze River region (Figure 2). This case-to-case variability in the SAT can be explained by the distinct anomalies of the circulation features associated with, for example, the Siberian high, the East Asia trough and/or the subtropical jet. In addition, the variability in the shape and magnitude of ESBs can contribute to the SAT variability as well. A discussion of the case-to-case variability of the SAT anomalies is beyond the scope of the present study.

Figure 3 shows the spatial distribution of the anomaly centers at the peak days for the three types of ESBs. The thick red, black and blue circles with crosses indicate the mean positions of the 54 cold-type, 14 neutral-type and 24 warm-type ESBs, respectively. Clearly, the warm-type ESBs tend to occur to the northwest of the cold-type ESBs, while the neutral-type ESBs tend to occur in between. In the following section, a comparison analysis between the cold and warm types of ESBs is performed.

Accepted for publication in *Monthly Weather Review*. DOI 10.1175/MWR-D-19-0152.1.

4 ESB Comparison Analysis

4.1 SLP and SAT Anomalies

The Siberian high represents the dominant weather system for the Eurasian continent near the surface in boreal winter, and it generally induces cold air outbreaks southeastward along the leeward slopes of the Tibetan Plateau (Tao 1957; Ding 1990). Climatologically, the northerlies associated with the Siberian high prevail across the region to the south of 40°N over East Asia and the Yangtze River region is subject to the influence of the anticyclonic high system (Figure 4).

Figure 5 shows the composite SLP anomalies, while Figure 6 shows the composite SAT anomalies. For the cold-type ESBs, on day -2 (Figure 5a), significant positive SLP anomalies appear over Eurasia with the primary center near the Ural Mountains. Because the center of the climatological mean Siberian high is located between Lake Balkhash and Lake Baikal (Figure 4), the positive anomalies shown in Figure 5a indicate that the Siberian high is amplified mainly in its northwestern portion. Correspondingly, a northwest-southeast tilting dipole pattern of SAT anomalies emerges on day -2 with significant positive anomalies centered over the Barents Sea and significant negative anomalies centered over Lake Balkhash (Figure 6a), resembling the “warm Arctic–cold Eurasian” pattern to some extent. Note that significant negative SAT anomalies cover the region around Lake Baikal. Takaya and Nakamura (2005b) revealed that the preexisting negative SAT anomalies around Lake

Accepted for publication in *Monthly Weather Review*. DOI 10.1175/MWR-D-19-0152.1.

Baikal contribute to the amplified Siberian high through their vertical interaction with upper-level wave train anomalies. The positive SLP anomalies are enhanced on day 0 (Figure 5b). Correspondingly, the dipole SAT anomalies are enhanced, and the majority of Asia is influenced by significant negative SAT anomalies (Figure 6b). On day 2, although the majority of the positive SLP anomalies still persist over the Ural Mountains, the central amplitude is weakened to approximately 18 hPa (Figure 5c). The positive SLP anomalies gradually extend southeastward along the northeastern slope of the Tibetan Plateau until day 6 (Figures 5c-5e). Correspondingly, the negative SAT anomalies gradually propagate southeastward along the northeastern slope of the Tibetan Plateau and persistently influence the Yangtze River region (Figures 6c-6e). After day 6 (not shown), the positive SLP anomalies gradually weaken and become nonsignificant, and the negative SAT anomalies over the Yangtze River region gradually weaken accordingly.

In contrast, for the warm-type ESBs, the Siberian high displays different features. Positive SLP anomalies occur on day -2 (Figure 5f) but are mainly limited to the region west of 75°E, with primary centers around the Scandinavian Peninsula, contributing to the formation of the significant positive SAT anomalies centered over the Barents–Kara Sea (Figure 6f). Negative SLP anomalies emerge over the region east of 75°E and become significant on day 0 with two primary centers around Lake Baikal (Figure 5g), reflecting the weakening of the Siberian high in the vicinity of its central portion. After day 0, these significant negative SLP anomalies gradually

Accepted for publication in *Monthly Weather Review*. DOI 10.1175/MWR-D-19-0152.1.

propagate southward and affect the Yangtze River region approximately from day 2 to day 4 (Figures 5h and 5i). Consequently, the Yangtze River region is influenced by significant persistent positive SAT anomalies from approximately day 2 to day 4 (Figures 6h and 6i), with a maximum central magnitude of approximately +4.5°C on day 4 (Figure 6i). On day 6, neither the SLP anomaly nor the SAT anomaly over the Yangtze River region are significant (Figures 5j and 6j).

Therefore, the cold-type ESBs are characterized by an anomalous Siberian high that mainly exhibits enhancement in its northwestern portion, while the warm-type ESBs are associated with an anomalous Siberian high that mainly shows weakening in its central portion. Both the positive and negative SLP anomalies associated with the anomalous Siberian high tend to propagate along the northeastern slope of the Tibetan Plateau. This result is consistent with the findings of Hsu (1987), who uncovered the anticyclonic propagation features of the SLP anomalies around the Tibetan Plateau based on lead-lag linear correlation analysis. In accordance with the evolution of the SLP anomalies, the SAT anomalies for both types of ESBs also propagate along the northeastern slope of the Tibetan Plateau.

4.2 Analysis on the Formation of Air Temperature Anomalies

To explore how the anomalous Siberian high induces the air temperature anomaly over the Yangtze River region, Figures 7a and 7e show the contributions from each term on the right hand side of Eq. (3), based on the composite fields and area-averaging over the Yangtze River region. Since the influence of the Siberian high

Accepted for publication in *Monthly Weather Review*. DOI 10.1175/MWR-D-19-0152.1.

is mainly confined to the lower troposphere, the 950 hPa level is chosen as the reference level at which all terms in Eq. (3) are evaluated.

For the cold type (Figure 7a), the tendency of the observed air temperature anomalies (thick black line) is negative overall before day 4, corresponding to the gradual enhancement of the negative SAT anomalies over the Yangtze River region (Figures 6a-6d). The tendency reaches the maximum on day 1 and becomes significant on day 1 and day 2. After day 4, the observed tendency becomes positive, indicating the weakening of the negative anomalies (Figure 6e). After decomposing the observed tendency, we find that the anomalous meridional temperature advection $-(v\partial T/\partial y)'$ (thick dashed red line in Figure 7a) is the primary contributor, which is significant after day -1. If $-(v\partial T/\partial y)'$ is further decomposed into $-(\bar{v}\partial T'/\partial y + v'\partial\bar{T}/\partial y) - (v'\partial T'/\partial y - \overline{v'\partial T'/\partial y})$, where the bar represents the climatological mean, the contribution of $-(v\partial T/\partial y)'$ mainly comes from that of $-v'\partial\bar{T}/\partial y$ (thin dashed red line in Figure 7a), which is significant after day 1. Thus, the anomalous meridional velocity v' associated with the anomalous Siberian high advects the climatological mean temperature southward, mainly explaining the formation of the negative temperature anomaly over the Yangtze River region for the cold-type ESBs. The diabatic heating term (solid blue line) is also significant after day -5 but mainly counteracts the cooling tendency over the Yangtze River region. The significant diabatic term mainly arises from longwave radiative heating and vertical diffusion heating (dashed blue line and dashed red line in Figure 7b). The remaining

Accepted for publication in *Monthly Weather Review*. DOI 10.1175/MWR-D-19-0152.1.

adiabatic terms are marginal, although the zonal advection term is significant on day -3 (dashed yellow line) and the vertical motion term is significant on day -5 and from day -2 to day 2 (dashed sky blue line).

The warm-type ESBs show a similar situation but with the opposite signs (Figure 7e). Specifically, the tendency of the observed air temperature anomalies (thick solid black line) becomes positive from day -3 to day 3. During this warming period, especially from day -2 to day 3, the term $-v'\partial\bar{T}/\partial y$ (thin dashed red line) is still the main contributor to the observed tendency of the air temperature, similar to its counterpart in the cold-type ESBs (Figure 7a). Both the zonal advection (dashed yellow line) term and the vertical motions term (dashed sky blue line) are significantly negative from approximately day 3 to day 5, contributing to the observed cooling tendency. Due to their relatively small amplitudes, the terms associated with the vertical motions are marginal in both the cold-type ESBs (Figure 7a) and the warm-type ESBs (Figure 7e), and we can also infer that the katabatic winds from the Tibetan Plateau and the subsidence in plains are not the primary contributors to the formation of the temperature anomalies over the Yangtze River region. The diabatic heating term is not significant (solid blue line in Figure 7e and Figure 7f) in the warm-type ESBs, which is different from the situation in the cold-type ESBs. This an asymmetric feature in the diabatic heating term deserves future study.

As seen in Figure 7e, the residual term seems to be not negligible for the warm-type ESBs, implying uncertainty in our budget analysis. As has been revealed,

Accepted for publication in *Monthly Weather Review*. DOI 10.1175/MWR-D-19-0152.1.

the meridional temperature advection terms, especially the term $-v'\partial\bar{T}/\partial y$, are the most important for the formation of the air temperature over the Yangtze River region. Thus, it is meaningful to check whether $-v'\partial\bar{T}/\partial y$ retains this importance if the errors are added. We assume that all the errors or the residual term are totally generated by $-v'\partial\bar{T}/\partial y$ while other terms are represented perfectly. Clearly, this approach artificially maximizes the errors caused by $-v'\partial\bar{T}/\partial y$ while eliminating the residual term. Our results show that, after having been adjusted by adding the residual term, the reduced $-v'\partial\bar{T}/\partial y$ still predominates over other terms, although it is significant only on day 1 (not shown). Thus, meridional temperature advection, especially $-v'\partial\bar{T}/\partial y$, is an important contributor to the formation of air temperature anomalies over the Yangtze River region for both types of ESBs.

To further check whether large case-to-case variability in $-v'\partial\bar{T}/\partial y$ occurs among the ESBs, Figure 7c shows the SLP anomaly, and Figure 7d shows $-v'\partial\bar{T}/\partial y$ at 950 hPa for each of the 54 cold-type ESBs. Clearly, the majority of the 54 cold-type ESBs are accompanied by a positive SLP anomaly over the Yangtze River region after day 2 and by a negative value of $-v'\partial\bar{T}/\partial y$ after day 1, which could be inferred from the significant results indicated by the red circles. A similar situation occurs for the warm-type ESBs but with the opposite sign from day 1 to day 3 (Figures 7g and 7h).

Therefore, the formation of the SAT anomalies over the Yangtze River region is mainly induced by the meridional advection of the climatological mean air

Accepted for publication in *Monthly Weather Review*. DOI 10.1175/MWR-D-19-0152.1.

temperature by the meridional wind velocity anomaly associated with the anomalous Siberian high. In addition, diabatic heating tends to counteract the local cooling tendency of air temperature over the Yangtze River region for cold-type ESBs.

4.3 Backward Trajectories

This section analyzes the differences in the trajectories of air parcels between the cold-type and warm-type ESBs, and qualitatively discusses whether diabatic or adiabatic processes are dominant during the movement of air parcels. Here, the 5-day backward trajectories are traced beginning on day 4 of each event at the reference grid point [115°E, 28.75°N] at the 950 hPa pressure level. Clearly, the grid point is close to the central grid point of the Yangtze River region. According to Eq. (4), the trajectory is derived from the total fields. Thus, in this section, we adopt a different point of view in exploring the formation of the SAT anomalies over the Yangtze River region from Section 4.2, which focuses on the local anomalous circulation.

As shown in Figure 8a for the 54 cold-type ESBs, the air parcels usually originate from the northern and northeastern Tibetan Plateau, as indicated by the filled blue circles. The parcels generally propagate along the northeastern slope of the Tibetan Plateau before they arrive at the Yangtze River region, exhibiting anticyclonic trajectories. Such consistent features among these trajectories could be attributable to the enhanced Siberian high because East Asia is still directly influenced by the enhanced Siberian high, which could regulate the trajectories of the air parcels. The red line in Figure 8a is the trajectory derived from the composite wind field associated

Accepted for publication in *Monthly Weather Review*. DOI 10.1175/MWR-D-19-0152.1.

with the 54 cold-type ESBs. Clearly, an anticyclonic trajectory is exhibited to the east of the Tibetan Plateau and corresponds to the representative trajectory for the cold-type ESBs.

For the 24 warm-type ESBs (Figure 8b), in contrast, the air parcels generally originate from the mid- and lower latitudes of East Asia and show diverse trajectories. Such diverse trajectories might be associated with the weakened Siberian high. Once the Siberian high is weakened over the Yangtze River region for the warm-type ESBs (Figures 5g-5i), the perturbations at mid- and lower latitudes might be more influential around the Yangtze River region, which might induce the diverse trajectories of the air parcels. Therefore, the trajectory derived from the composite wind velocity field for the 24 warm-type ESBs (red line in Figure 8b) cannot be regarded as the representative trajectory for the warm-type ESBs.

Figure 8c displays the air temperature-potential temperature diagram for the air parcels during their movement for the cold-type ESBs. Overall, the polylines that connect the origins (blue circles) to the reference points (blue asterisks) tend to extend more along the Y-axis than along the X-axis. This pattern could be easily inferred from the trajectory derived from the composite field for the cold-type ESBs (red line in Figure 8c). In other words, the changes in the air temperature tend to be larger than the changes in the potential temperature during the movement of the air parcels associated with the 54 cold-type ESBs. This result indicates that adiabatic processes

Accepted for publication in *Monthly Weather Review*. DOI 10.1175/MWR-D-19-0152.1.

are more important during the movement of air parcels associated with cold-type ESBs.

For the 24 warm-type ESBs, consistent with the diverse trajectories of the air parcels, the variations in the temperature and the potential temperature also show large case-to-case variability (Figure 8d). Some cases are characterized by a primarily diabatic process, while others are characterized by a primarily adiabatic process. The thick red line in Figure 8d, which is obtained from the composite field, can hardly be representative of the overall situation for warm-type ESBs.

4.4 Low-frequency Rossby Wave Propagation

In the upper troposphere (300 hPa) on day -4 for the cold-type ESBs (Figure 9a), significant negative height anomalies occur over Western Europe, while positive height anomalies are anchored around the Kara Sea and Taymyr Peninsula. Indeed, this circulation pattern emerges on day -5, and no significant circulation anomaly can be observed farther upstream (not shown). The stationary Rossby wave packets from Western Europe propagate northeastward to the Ural Mountains and are then reflected southeastward, after which they finally converge around Lake Baikal. Corresponding to the downstream dispersion of wave energy along the arc-shaped path, from day -2 (Figure 9b) to day 0 (Figure 9c), the cyclonic anomalies over Western Europe gradually weaken, while both the anticyclonic anomalies centered over the Ural Mountains and the cyclonic anomalies to the southwest of Lake Baikal gradually strengthen. The anticyclonic anomalies centered over the Ural Mountains have the

Accepted for publication in *Monthly Weather Review*. DOI 10.1175/MWR-D-19-0152.1.

strongest amplitude among the wave train anomalies over the Eurasian continent. Some studies have emphasized the role of upstream cyclogenesis in the enhancement of blocking highs through the poleward advection of anticyclonic vorticity and warm air (Colucci 1985; Cheung et al. 2013); this finding is also implied here by the cyclonic anomalies over Western Europe (Figures 9a and 9b). On the other hand, from a potential vorticity-inversion perspective, the enhanced anticyclonic anomalies might also be associated with the local coupling between the upper-level anticyclonic anomalies and the negative SAT anomalies around Lake Baikal (Takaya and Nakamura 2005b). After day 0 (Figures 9d and 9e), the height anomalies gradually weaken. However, the wave-activity fluxes mainly emanate from the anticyclonic anomalies over the Ural Mountains and converge over the region from Central Asia to East Asia. Correspondingly, the cyclonic anomalies over midlatitude East Asia weaken at a much more gradual rate than the anticyclonic anomalies over the Ural Mountains (Figures 9e). During the evolution of the cold-type ESBs, the dipole of geopotential height anomalies tilts over the Eurasian continent in the northwest-southeast direction, which is a typical feature of persistent cold events over China (Bueh et al. 2011a; Bueh et al. 2011b) and midlatitude Asia (Shi et al. 2019).

For the warm-type ESBs, on day -4 (Figure 9f), significant cyclonic anomalies around southern Greenland can be traced back to as far as day -6 (not shown). Rossby wave packets emanate from these cyclonic anomalies and propagate eastward, together with the northward propagation of Rossby wave packets from Eastern

Accepted for publication in *Monthly Weather Review*. DOI 10.1175/MWR-D-19-0152.1.

Europe, contributing to the enhancement of the anticyclonic anomalies centered around the northern Scandinavian Peninsula and Barents Sea from day -4 (Figure 9f) to day 0 (Figure 9h). Therefore, this finding is basically consistent with the finding of Tyrlis and Hoskins (2008) that the onset of blocking highs over Europe is generally preceded by the existence of cyclonic anomalies to the west of Greenland. Although the zonal extents of the primary anticyclonic anomalies are comparable between the two types of ESBs on day 0, i.e., 90°, the center of the primary anticyclonic height anomaly associated with the warm-type ESBs is located slightly northwest of its counterpart. Such differences in the locations of these primary anticyclonic anomaly centers for the two types of ESBs might be related to the different preexisting circulation anomalies located upstream and the different propagation patterns of the associated Rossby waves. After day 0 (Figures 9h-9j), the wave-activity fluxes begin to diverge around the Ural Mountains and propagate both eastward and southeastward. The convergence of wave-activity flux is favorable for the enhancement and maintenance of the downstream cyclonic anomalies around Lake Baikal and the Caspian Sea. Thus, consistent with the northwest displacement of the primary anticyclonic height anomaly of the warm-type ESBs, the cyclonic anomaly around Lake Baikal is also located to the northwest of its cold-type ESBs counterpart.

Joung and Hitchman (1982) and Takaya and Nakamura (2005a) revealed that cold air outbreaks or cold anomalies over East Asia are accompanied by wave trains across the Eurasian continent. The wave train anomalies mainly show a barotropic

Accepted for publication in *Monthly Weather Review*. DOI 10.1175/MWR-D-19-0152.1.

structure across most of Eurasia but become baroclinic when they approach the coast of East Asia. Inspired by their studies, we also analyze the vertical structures of the primary height anomalies over the Eurasian continent for both types of ESBs (not shown). Our results are basically consistent with those of early studies (Joung and Hitchman1982; Takaya and Nakamura 2005a) insomuch that both types of ESBs generally demonstrate a barotropic structure across most of Eurasia, which pertains to the evident horizontal propagation of Rossby waves in the troposphere. Moreover, the baroclinic structure of the wave trains over East Asia is also evident for both the cold-type and warm-type ESBs, with the height anomalies tilting northwestward with height (not shown).

4.5 Relationships with Teleconnection Patterns

One of the notable circulation differences between the two types of ESBs is the locations of the primary geopotential height anomalies, and these discrepancies appear to be related to differences in the large-scale teleconnection patterns. Figure 10 shows the composite daily teleconnection pattern indices during the evolution of the ESBs. Evidently, the cold-type ESBs are closely associated with a significant positive index of the East Atlantic/West Russia pattern from day -10 to day 7 (Figure 10a). The East Atlantic/West Russia pattern in its positive phase consists of one anticyclonic anomaly center around the Ural Mountains and two cyclonic anomaly centers around Western Europe and Northeast China (Barnston and Livezey, 1987). During the evolution of the cold-type ESBs, the significant height anomalies associated with the

Accepted for publication in *Monthly Weather Review*. DOI 10.1175/MWR-D-19-0152.1.

cyclonic anomaly over Western Europe before day -2 (Figures 9a and 9b), the primary anticyclonic anomaly around the Ural Mountains (left column of Figure 9), and the significant cyclonic anomalies around Northeast China after day 2 (Figures 9d and 9e) resemble the positive East Atlantic/West Russia pattern. The North Atlantic Oscillation (red line) does not exhibit consistent variation during the evolution of the cold-type ESBs, as was also hinted by Luo et al. (2016b).

In contrast, for the warm-type ESBs, both the East Atlantic/West Russia and Scandinavian patterns become relevant from approximately day -2 to day 5 (Figure 10b). The positive East Atlantic/West Russia pattern generally has one primary anticyclonic anomaly center over the Scandinavian Peninsula and one primary cyclonic center around Lake Baikal (Barnston and Livezey, 1987; Bueh and Nakamura, 2007). For the warm-type ESBs, the primary anticyclonic height anomaly around the Scandinavian Peninsula extends zonally and gradually covers the Ural Mountains (Figures 9f-9j), and a cyclonic height anomaly forms around Lake Baikal after day -2 (Figures 9h-9j), together indicating a mixture of the East Atlantic/West Russia and East Atlantic/West Russia pattern patterns.

5 Conclusions and Discussion

Based on JRA-55 reanalysis data, 54 cold-type ESBs and 24 warm-type ESBs are selected according to their influences on the SAT anomalies over the Yangtze River region. We find that warm-type ESBs tend to occur relatively northwestward of

Accepted for publication in *Monthly Weather Review*. DOI10.1175/MWR-D-19-0152.1.

cold-type ESBs. As inferred from the anomalous SLP field, the Siberian high is weakened for warm-type ESBs and enhanced for cold-type ESBs over the Yangtze River region. The anomalous Siberian high can induce the advection of climatological mean air temperature by anomalous meridional wind velocities in the lower troposphere, which is the main contributor to the air temperature anomalies in both ESB types. In addition, diabatic heating tends to counteract the local air temperature cooling tendency over the Yangtze River region in the cold-type ESBs.

Noticeable differences are also observed in the mid- and upper-level anomalous circulations between the two types of ESBs. The cold-type ESBs are characterized by height anomalies with a northwest-southeast tilting dipole structure over the Eurasian continent on their peak day, which is consistent with the propagation of Rossby wave packets along an arc-shaped path over the Eurasian continent. Indeed, the typical features of the cold-type ESBs are generally consistent with the wave train that crosses the Eurasian continent in association with the Ural blocking highs (Takaya and Nakamura, 2005a; Cheung et al., 2012; Luo et al. 2016b). The circulation anomalies of the cold-type ESBs resemble the East Atlantic/West Russia pattern in its positive phase. In contrast, the height anomalies of the warm-type ESBs over the Eurasian continent are located to the northwest of their cold-type ESB counterparts. In addition to the positive East Atlantic/West Russia teleconnection pattern, the Scandinavian teleconnection pattern also becomes significant during the evolution of the warm-type ESBs.

Accepted for publication in *Monthly Weather Review*. DOI 10.1175/MWR-D-19-0152.1.

In addition to the anomaly fields, differences occur in the total fields between the two types of ESBs. In the cold-type ESBs, the air parcels in the lower troposphere over the Yangtze River region on day 4 generally originate from the regions to the north and northeast of the Tibetan Plateau, and an adiabatic process is dominant during the motion of the air parcels. In contrast, in the warm-type ESBs, the air parcels generally originate from the mid- and low latitudes of East Asia and exhibit diverse trajectories.

We also test the sensitivity of the results to minor changes in the criteria for either defining an ESB or classifying the types of ESBs, as shown in Section 2.2.2, and check whether the thermodynamic features over the Yangtze River region, as revealed in sections 4.2 and 4.3, change obviously if the spatial location of the reference grid point is shifted slightly. Specifically, for the identification of an ESB, we change the requirement for the minimum longitudinal extent of the instantaneous local blocking to 10° or 17.5°, the minimum duration to 5 days, or the minimum magnitude of the primary height anomaly to 15 gpdm on the peak day. The SAT anomalies are averaged over different periods, e.g., from day 2 to day 4 or from day 2 to day 5, based on classification of the ESBs. In the results, the typical features of the cold-type and warm-type ESBs do not change qualitatively, but the significance weakens when fewer cases are identified for the composite analysis (not shown). In addition, the results of the formation of the air temperature anomaly over the Yangtze River region still do not change qualitatively if Eq. (3) is calculated at 975 hPa or if

Accepted for publication in *Monthly Weather Review*. DOI 10.1175/MWR-D-19-0152.1.

other starting points, e.g., [117.5°E, 32.5°N], [117.5°E, 25°N] and [110°E, 28.75°N], are used for tracking the backward trajectories.

Early studies recognized that migratory synoptic eddies play an important role in the maintenance of blocking highs (Green 1977; Illari and Marshall 1983; Shutts 1983; Colucci 1985; Holopainen and Fortelius 1987; Mullen 1987; Nakamura et al. 1997; Tsou and Smith 1990). Furthermore, Han et al. (2011) noted that warm sea surface temperature anomalies over the North Atlantic are favorable for strengthening the blocking highs over the Ural Mountains by modulating transient eddy activities. We have also evaluated the instantaneous baroclinic wave activity, as in Nakamura et al. (1997), and its feedback forcing through the convergence of the heat flux and vorticity flux, as in Lau and Holopainen (1984). Although the cold-type ESBs are associated with significantly enhanced transient eddy activities over the Kara Sea and reduced transient eddy activities around the Ural Mountains, the eddy forcing in the mid- and upper troposphere is marginally significant for both types of ESBs (not shown), indicating high case-to-case variability. The evolution of blocking highs is generally associated with both high- and low-frequency dynamics (Nakamura et al. 1997). The former can be diagnosed by transient eddy feedback forcing, while the latter can be represented by low-frequency Rossby wave propagation. Therefore, the lack of significant signals of the transient eddy feedback forcing implies that low-frequency Rossby wave propagation plays an important role in both types of ESBs.

Accepted for publication in *Monthly Weather Review*. DOI 10.1175/MWR-D-19-0152.1.

Wang et al. (2010) showed that the stationary wave propagation associated with Ural blocking highs differed considerably between the period from 1957 to 1976 and the period from 1977 to 2000. Furthermore, the frequency of Ural blocking highs showed an increasing trend after the 1990s (Barnes et al. 2014; Wang and Chen 2014). Therefore, it is worth analyzing the dynamics of blocking highs during periods with high and low Ural blocking frequencies. In addition, Arctic sea ice loss (Honda et al. 2009; Liu et al. 2012; Mori et al. 2014; Luo et al. 2016a) and cooling over the eastern Pacific (Han et al. 2016) might contribute to the formation of anticyclonic anomalies around the Ural Mountains, which could advect warm air masses poleward and cold air masses equatorward, thereby enhancing the warm Arctic–cold Eurasia pattern (Luo et al. 2016a). The role of external forcings in the long-term variations in both the different ESB types and the SAT over Eurasia also deserves a dedicated further investigation.

Acknowledgments

This work was supported jointly by the National Key R&D Program of China (Grant No. 2016YFA0600702), National Science-technology Support Plan Projects (Grant No. 2015BAC03B03), the Chinese Natural Science Foundation (41575057) and the Funding of Jiangsu Innovation & Entrepreneurship Team. The National Center for Atmospheric Research NCAR Command Language (NCL) was used to perform the calculations and draw the plots.

Accepted for publication in *Monthly Weather Review*. DOI 10.1175/MWR-D-19-0152.1.

References

Baldwin, M. P., T. J. Dunkerton, 2001: Stratospheric Harbingers of Anomalous Weather Regimes. *Science*, **294,** 581–584. doi: 10.1126/science.1063315.

Barnes, E. A., E. Dunn‐Sigouin, G. Masato, and T. Woollings, 2014: Exploring recent trends in Northern Hemisphere blocking. *Geophysical Research Letters*, **41,** 638–644, doi: 10.1002/2013GL058745.

Barnston, A. G., and R. E. Livezey, 1987: Classification, Seasonality and Persistence of Low-Frequency Atmospheric Circulation Patterns. *Monthly Weather Review*, **115,** 1083–1126, doi: 10.1175/1520-0493(1987)115<1083:csapol>2.0.co;2.

Barriopedro, D., R. García-Herrera, and R. Trigo, 2010: Application of blocking diagnosis methods to General Circulation Models. Part I: a novel detection scheme. *Climate Dynamics*, **35,** 1373–1391, doi: 10.1007/s00382-010-0767-5.

Barriopedro, D., R. García-Herrera, A. R. Lupo, and E. Hernández, 2006: A Climatology of Northern Hemisphere Blocking. *Journal of Climate*, **19,** 1042–1063, doi: 10.1175/JCLI3678.1.

Accepted for publication in *Monthly Weather Review*. DOI 10.1175/MWR-D-19-0152.1.

Bueh, C., and H. Nakamura, 2007: Scandinavian pattern and its climatic impact. *Quarterly Journal of the Royal Meteorological Society*, **133,** 2117–2131, doi:10.1002/qj.173.

Bueh, C., N. Shi, and Z. Xie, 2011a: Large-scale circulation anomalies associated with persistent low temperature over Southern China in January 2008. *Atmospheric Science Letters*, **12,** 273–280, doi: 10.1002/asl.333.

Bueh, C., X.-Y. Fu, and Z.-W. Xie, 2011b: Large-scale circulation features typical of wintertime extensive and persistent low temperature events in China. *Atmospheric and Oceanic Science Letters*, **4,** 235–241, doi:10.1080/16742834.2011.11446935.

Cheung, H. N., W. Zhou, H. Y. Mok, and M. C. Wu, 2012: Relationship between Ural–Siberian Blocking and the East Asian Winter Monsoon in Relation to the Arctic Oscillation and the El Niño–Southern Oscillation. *Journal of Climate*, **25,** 4242–4257, doi:10.1175/jcli-d-11-00225.1.

Cheung, H. N., and coauthors, 2013: Observational climatology and characteristics of wintertime atmospheric blocking over Ural–Siberia. *Climate Dynamics*, **41,** 63–79, doi:10.1007/s00382-012-1587-6.

Colucci, S. J., 1985: Explosive Cyclogenesis and Large-Scale Circulation Changes: Implications for Atmospheric Blocking. *Journal of Atmospheric Sciences*,

Accepted for publication in *Monthly Weather Review*. DOI 10.1175/MWR-D-19-0152.1.

42, 2701–2717, doi: 10.1175/1520-0469(1985)042<2701:ECALSC>2.0.CO;2.

Ding, Y., 1990: Build-up, air mass transformation and propagation of Siberian high and its relations to cold surge in East Asia. *Meteorology & Atmospheric Physics*, **44,** 281–292, doi: 10.1007/BF01026822.

Ding, Y., and T. N. Krishnamurti, 1987: Heat Budget of the Siberian High and the Winter Monsoon. *Monthly Weather Review,* **115,** 2428–2449, doi:10.1175/1520-0493(1987)115<2428:hbotsh>2.0.co;2.

Dole, R. M., and N. D. Gordon, 1983: Persistent anomalies of the extratropical Northern Hemisphere wintertime circulation: Geographical distribution and regional persistence characteristics. *Monthly Weather Review,* **111,** 1567–1586, doi:10.1175/1520-0493(1983)111%3C1567:PAOTEN%3E2.0.CO;2.

Green, J. S. A., 1977: The weather during July 1976: Some dynamical considerations of the drought. *Weather,* **32,** 120–128, doi:10.1002/j.1477-8696.1977.tb04532.x.

Han, Z., S. Li, and M. Mu, 2011: The role of warm North Atlantic SST in the formation of positive height anomalies over the Ural Mountains during January 2008. *Advances in Atmospheric Sciences*, **28,** 246–256, doi:10.1007/s00376-010-0069-1.

Accepted for publication in *Monthly Weather Review*. DOI 10.1175/MWR-D-19-0152.1.

Han, Z., S. Li, J. Liu, Y. Gao, and P. Zhao, 2016: Linear Additive Impacts of Arctic Sea Ice Reduction and La Niña on the Northern Hemisphere Winter Climate. *Journal of Climate,* **29,** 5513–5532, doi:10.1175/jcli-d-15-0416.1.

Holopainen, E., and C. Fortelius, 1987: High-frequency transient eddies and blocking. *Journal of the Atmospheric Sciences*, **44,** 1632–1645, doi:10.1175/1520-0469(1987)0442.0.CO;2.

Holton, J. R., 2004: An Introduction to Dynamic Meteorology. 4th ed. Elsevier Academic Press, 535 pp.

Horel, J., 1981: A rotated principal component analysis of the interannual variability of the Northern Hemisphere 500 mb height field. *Monthly Weather Review,* **109,** 2080–2092. doi:10.1175/1520-0493(1981)1092.0.CO;2.

Hsu, H.-H., 1987: Propagation of Low-Level Circulation Features in the Vicinity of Mountain Ranges. *Monthly Weather Review,* **115,** 1864–1893, doi:10.1175/1520-0493(1987)115<1864:pollcf>2.0.co;2.

Illari, L., and J. C. Marshall, 1983: On the Interpretation of Eddy Fluxes During a Blocking Episode. *Journal of the Atmospheric Sciences*, **40,** 2232–2242, doi:10.1175/1520-0469(1983)040<2232:otioef>2.0.co;2.

Joung, C. H., and M. H. Hitchman, 1982: On the Role of Successive Downstream Development in East Asian Polar Air Outbreaks. *Monthly Weather Review*, **110,** 1224, doi:10.1175/1520-0493(1982)110<1224:OTROSD>2.0.CO;2.

Accepted for publication in *Monthly Weather Review*. DOI 10.1175/MWR-D-19-0152.1.

Knox, J., and J. Hay, 1984: Blocking signatures in the Northern Hemisphere: Rationale and identification. *Atmosphere,* **22,** 36–47, doi:10.1080/07055900.1984.9649183.

Kobayashi, S., and coauthors, 2015: The JRA-55 Reanalysis: General Specifications and Basic Characteristics. *Journal of the Meteorological Society of Japan. Ser. II*, **93,** 5–48, doi:10.2151/jmsj.2015-001.

Lau, N.-C., and E. O. Holopainen, 1984: Transient eddy forcing of the time-mean flow as identified by geopotential tendencies. *Journal of the Atmospheric Sciences*, **41,** 313–328, doi:10.1175/1520-0469(1984)041%3C0313:TEFOTT%3E2.0.CO;2.

Lau, N.-C., and M. J. Nath, 1991: Variability of the baroclinic and barotropic transient eddy forcing associated with monthly changes in the midlatitude storm tracks. *Journal of the Atmospheric Sciences*, **48,** 2589–2613, doi:10.1175/1520-0469(1991)048<2589:VOTBAB>2.0.CO;2.

Liu, J., J. A. Curry, H. Wang, M. Song, and R. M. Horton, 2012: Impact of declining Arctic sea ice on winter snowfall. *Proceedings of the National Academy of Sciences of the United States of America*, **109,** 4074–4079, doi:10.1073/pnas.1114910109.

Accepted for publication in *Monthly Weather Review*. DOI 10.1175/MWR-D-19-0152.1.

Luo, D., and coauthors, 2016a: Impact of Ural Blocking on Winter Warm Arctic–Cold Eurasian Anomalies. Part I: Blocking-Induced Amplification. *Journal of Climate*, **29,** 3925–3947, doi:10.1175/jcli-d-15-0611.1.

Luo, D., and coauthors, 2016b: Impact of Ural Blocking on Winter Warm Arctic–Cold Eurasian Anomalies. Part II: The Link to the North Atlantic Oscillation. *Journal of Climate*, **29,** 3949–3971, doi:10.1175/jcli-d-15-0612.1.

Lupo, A. R., and P. J. Smith, 1995: Climatological features of blocking anticyclones in the Northern Hemisphere. *Tellus*, **47A,** 439–456, doi:10.3402/tellusa.v47i4.11527.

Masato, G., B. J. Hoskins, and T. J. Woollings, 2011: Wave-breaking characteristics of midlatitude blocking. *Quarterly Journal of the Royal Meteorological Society*, **138,** 1285–1296, doi:10.1002/qj.990.

Matsueda, M., and T. N. Palmer, 2018: Estimates of flow-dependent predictability of wintertime Euro-Atlantic weather regimes in medium-range forecasts. *Quarterly Journal of the Royal Meteorological Society*, **144,** 1012–1027, doi:10.1002/qj.3265.

Mori, M., M. Watanabe, H. Shiogama, J. Inoue, and M. Kimoto, 2014: Robust Arctic sea-ice influence on the frequent Eurasian cold winters in past decades. *Nature Geoscience*, **7,** 869–873, doi:10.1038/ngeo2277.

Accepted for publication in *Monthly Weather Review*. DOI 10.1175/MWR-D-19-0152.1.

Mullen, S. L., 1987: Transient eddy forcing of blocking flows. *Journal of Atmospheric Sciences*, **44,** 3–22, doi:10.1175/1520-0469(1987)044<0003:TEFOBF>2.0.CO;2.

Nakamura, H., 1992: Midwinter Suppression of Baroclinic Wave Activity in the Pacific. *Journal of the Atmospheric Sciences*, **49,** 1629–1642, doi:10.1175/1520-0469(1992)049<1629:msobwa>2.0.co;2.

Nakamura, H., 1994: Rotational evolution of potential vorticity associated with a strong blocking flow configuration over Europe. *Geophysical Research Letters*, **21,** 2003–2006, doi:10.1029/94GL01614.

Nakamura, H., M. Nakamura, and J. L. Anderson, 1997: The Role of High-and Low-Frequency Dynamics in Blocking Formation. *Monthly Weather Review*, **125,** 2074–2093, doi:10.1029/94GL01614.

Overland, J. E., K. Wood, R., and M. Wang, 2011: Warm Arctic—cold continents: climate impacts of the newly open Arctic Sea. *Polar Research*, **30,** 15787, doi:10.3402/polar.v30i0.15787.

Pelly, J. L., and B. J. Hoskins, 2003: A New Perspective on Blocking. *Journal of the Atmospheric Sciences*, **60,** 743–755, doi:10.1175/1520-0469(2003)060<0743:ANPOB>2.0.CO;2.

Accepted for publication in *Monthly Weather Review*. DOI 10.1175/MWR-D-19-0152.1.

Shi, N., X. Wang, and P. Tian, 2019: Interdecadal variations in persistent anomalous cold events over Asian mid-latitudes. *Climate Dynamics*, **52,** 3729–3739, doi:10.1007/s00382-018-4353-6.

Shutts, G. J., 1983: The propagation of eddies in diffluent jetstreams: Eddy vorticity forcing of ‘blocking’ flow fields. *Quarterly Journal of the Royal Meteorological Society*, **109,** 737–761, doi: 10.1002/qj.49710946204.

Takaya, K., and H. Nakamura, 1997: A formulation of a wave-activity flux for stationary Rossby waves on a zonally varying basic flow. *Geophysical Research Letters*, **24,** 2985–2988, doi: 10.1029/97GL03094.

Takaya, K., and H. Nakamura, 2001: A formulation of a phase-Independent wave-activity flux for stationary and migratory quasigeostrophic eddies on a zonally varying basic flow. *Journal of the Atmospheric Sciences*, **58,** 608–627, doi:10.1175/1520-0469(2001)058,0608:AFOAPI.2.0.CO;2.

Takaya, K., and H. Nakamura, 2005a: Geographical Dependence of Upper-Level Blocking Formation Associated with Intraseasonal Amplification of the Siberian High. *Journal of the Atmospheric Sciences*, **62,** 4441–4449, doi: 10.1175/JAS3628.1.

Takaya, K., and H. Nakamura, 2005b: Mechanisms of Intraseasonal Amplification of the Cold Siberian High. *Journal of the Atmospheric Sciences*, **62,** 4423–4440, doi:10.1175/JAS3629.1.

Accepted for publication in *Monthly Weather Review*. DOI 10.1175/MWR-D-19-0152.1.

Tao, S., 1957: *A study of activities of cold airs in East Asian winter, handbook of short-term forecast (in Chinese), China Meteorological Administration*. Meteorology Press.

Tao, S., and J. Wei, 2008: Severe snow and freezing-rain in January 2008 in the Southern China. *Climatic and Environmental Research (in Chinese)*, **13,** 337–350, doi:10.3878/j.issn.1006-9585.2008.04.01.

Tibaldi, S., and F. Molteni, 1990: On the operational predictability of blocking. *Tellus*, **42A,** 343–365, doi:10.1034/j.1600-0870.1990.t01-2-00003.x.

Tibaldi, S., E. Tosi, A. Navarra, and L. Pedulli, 1994: Northern and Southern Hemisphere seasonal variability of blocking frequency and predictability. *Monthly Weather Review*, **122,** 1971–2003, doi:10.1175/1520-0493(1994)122%3C1971:NASHSV%3E2.0.CO;2.

Tsou, C.-H., and P. J. Smith, 1990: The role of synoptic/planetary-scale interactions during the development of a blocking anticyclone. *Tellus A: Dynamic Meteorology and Oceanography*, **42,** 174–193, doi:10.3402/tellusa.v42i1.11869.

Tyrlis, E., and B. J. Hoskins, 2008: The Morphology of Northern Hemisphere Blocking. *Journal of the Atmospheric Sciences*, **65,** 1653–1665, doi:10.1175/2007JAS2338.1.

Accepted for publication in *Monthly Weather Review*. DOI 10.1175/MWR-D-19-0152.1.

Wallace, J. M., D. S. Gutzler, 1981: Teleconnections in the geopotential height field during the Northern Hemisphere winter. *Monthly Weather Review*, **109,** 784–812. doi:10.1175/1520-0493(1981)109,0784:TITGHF.2.0.CO;2.

Wang, L., and coauthors, 2010: Effect of the climate shift around mid 1970s on the relationship between wintertime Ural blocking circulation and East Asian climate. *International Journal of Climatology*, **30,** 153–158, doi:10.1002/joc.1876.

Wang, L., and W. Chen, 2014: The East Asian winter monsoon:re-amplification in the mid-2000s. *Chinese Science Bulletin*, 59**,** 430–436, doi:10.1007/s11434-013-0029-0.

Wen, M., S. Yang, A. Kumar, and P. Zhang, 2009: An Analysis of the Large-Scale Climate Anomalies Associated with the Snowstorms Affecting China in January 2008. *Monthly Weather Review*, **137,** 1111–1131, doi:10.1175/2008mwr2638.1.

Wernli, B. H., and H. C. Davies, 1997: A lagrangian-based analysis of extratropical cyclones. I: The method and some applications. *Quarterly Journal of the Royal Meteorological Society*, **123,** 467–489, doi:10.1002/qj.49712353811.

Wiedenmann, J. M., A. R. Lupo, I. I. Mokhov, and E. A. Tikhonova, 2002: The Climatology of Blocking Anticyclones for the Northern and Southern

Accepted for publication in *Monthly Weather Review*. DOI 10.1175/MWR-D-19-0152.1.

Hemispheres: Block Intensity as a Diagnostic. *Journal of Climate*, **15,** 3459–3473, doi:10.1175/1520-0442(2002)015<3459:TCOBAF>2.0.CO;2.

Wilks, D. S., 2016: “The Stippling Shows Statistically Significant Grid Points”: How Research Results are Routinely Overstated and Overinterpreted, and What to Do about It. *Bulletin of the American Meteorological Society*, **97,** 2263–2273, doi:10.1175/bams-d-15-00267.1.

Zschenderlein, P., G. Fragkoulidis, A. H. Fink, and V. Wirth, 2018: Large-scale Rossby wave and synoptic-scale dynamic analyses of the unusually late 2016 heatwave over Europe. *Weather*, **73,** 275–283, doi:10.1002/wea.3278.

Zhou, W., and coauthors, 2009: Synoptic-Scale Controls of Persistent Low Temperature and Icy Weather over Southern China in January 2008. *Monthly Weather Review*, **137**, 3978–3991, doi:10.1175/2009mwr2952.1.

Accepted for publication in *Monthly Weather Review*. DOI 10.1175/MWR-D-19-0152.1.

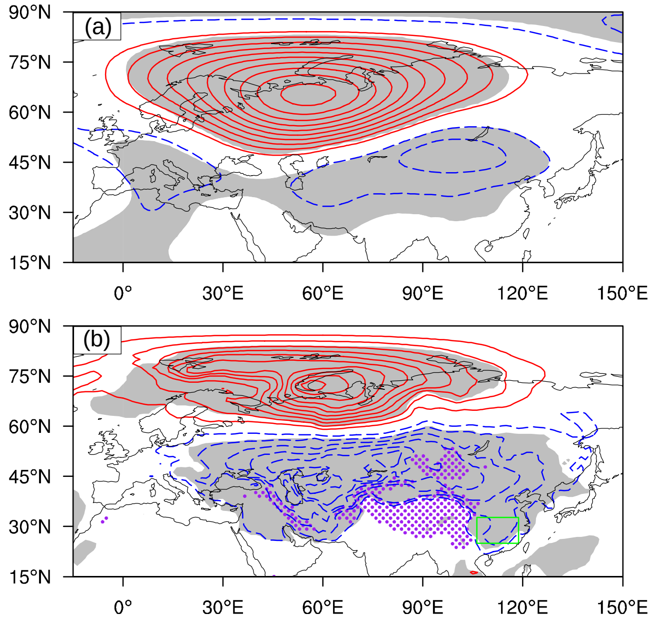

Figure 1 Composite of the 7-day mean circulation anomalies of 92 ESBs. (a) Geopotential height at 500 hPa (units: gpdm) averaged from day -3 to day 3 and (b) is the SAT (units: ℃) averaged from day 1 to day 7. Contours are drawn for ±2, ±4, …… gpdm in (a) and ±0.75, ±1.5, …… ℃ in (b). Red solid and blue dashed lines represent the positive and negative values, respectively. The shading denotes the significant anomalies based on Student's *t* tests with false discovery rates controlled by p^{*}_{FDR} ≈1.1% and 0.5% for (a) and (b), respectively, computed with α_{FDR} =0.05. Purple stippling indicates a topographic height exceeding 1500 m. Green rectangle in Figure 1b represents the Yangtze River region.

Accepted for publication in *Monthly Weather Review*. DOI 10.1175/MWR-D-19-0152.1.

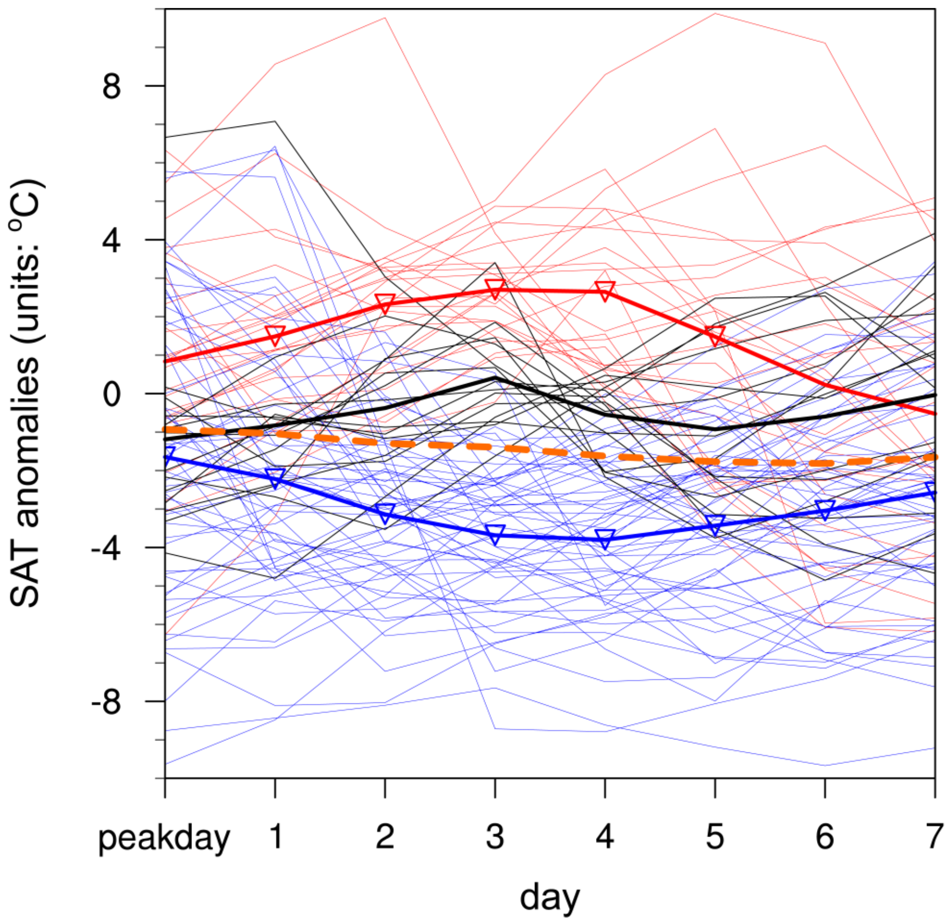

Figure 2 Area-averaged SAT anomalies (°C) over the Yangtze River region (green rectangle in Figure 1b) after the peak days of the 92 ESBs. For the abscissa, “0” represents the peak day of an ESB, and the numbers represent the days after the peak day. The thin blue lines, thin black lines and thin red lines represent the ESB events with the area-averaged SAT anomalies averaged over the period from day 3 to day 4 below -1°C, between -1°C and 1°C, and above 1°C, respectively. The thick lines are the averages of the thin lines with the same color. The thick orange dashed line represents the average of all 92 ESBs. The inverted triangles denote significant averages according to Student’s *t* test with false discovery rates controlled by $p^{*}_{\mathrm{FDR}} \approx$1.0% and 0.2% for the cold-type ESBs and the warm-type ESBs, respectively, computed with α_{FDR} =0.05.

Accepted for publication in *Monthly Weather Review*. DOI 10.1175/MWR-D-19-0152.1.

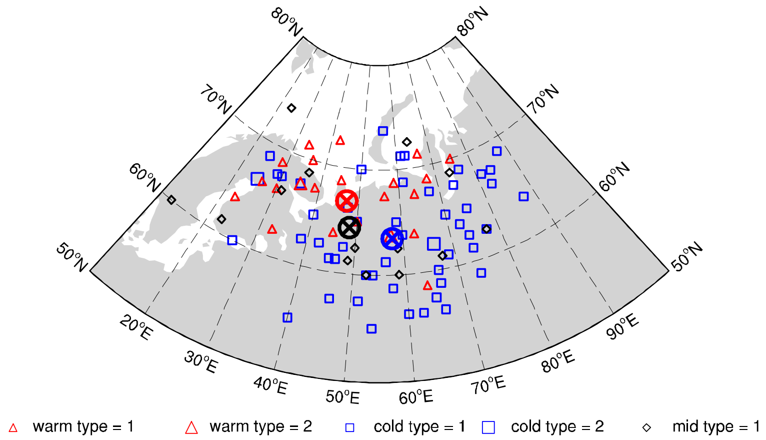

Figure 3 Distribution of anomaly centers on the peak day for the 54 cold-type ESBs (blue rectangles), 14 neutral-type ones (black asterisks) and 24 warm-type ones (red triangles). The times at which the anomaly centers of the ESBs are located at every grid point are indicated at the bottom of the figure. The big markers imply that two BHs were centered at this grid point. The thick red, black and blue circles with cross indicate the mean position of the warm-type, neutral-type and cold-type ESBs, respectively.

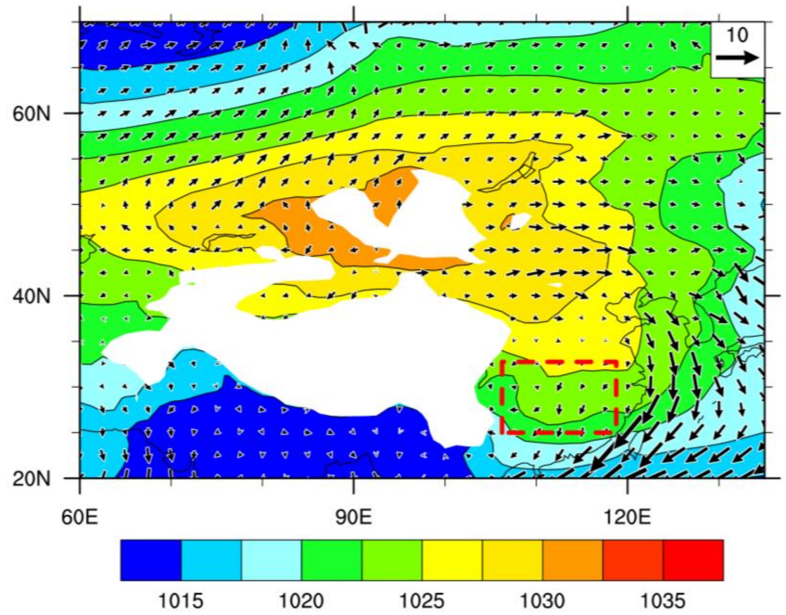

Figure 4 Extended boreal winter (November to March) climatological mean sea level pressure (shading, unit: hPa) and wind velocity (vectors, units: m/s) at 1000 hPa. The white shading represents the region where the topographic height exceeds 1500 m. The red dashed rectangle represents the Yangtze River region. The wind velocity scale is plotted at the top right of the panel.

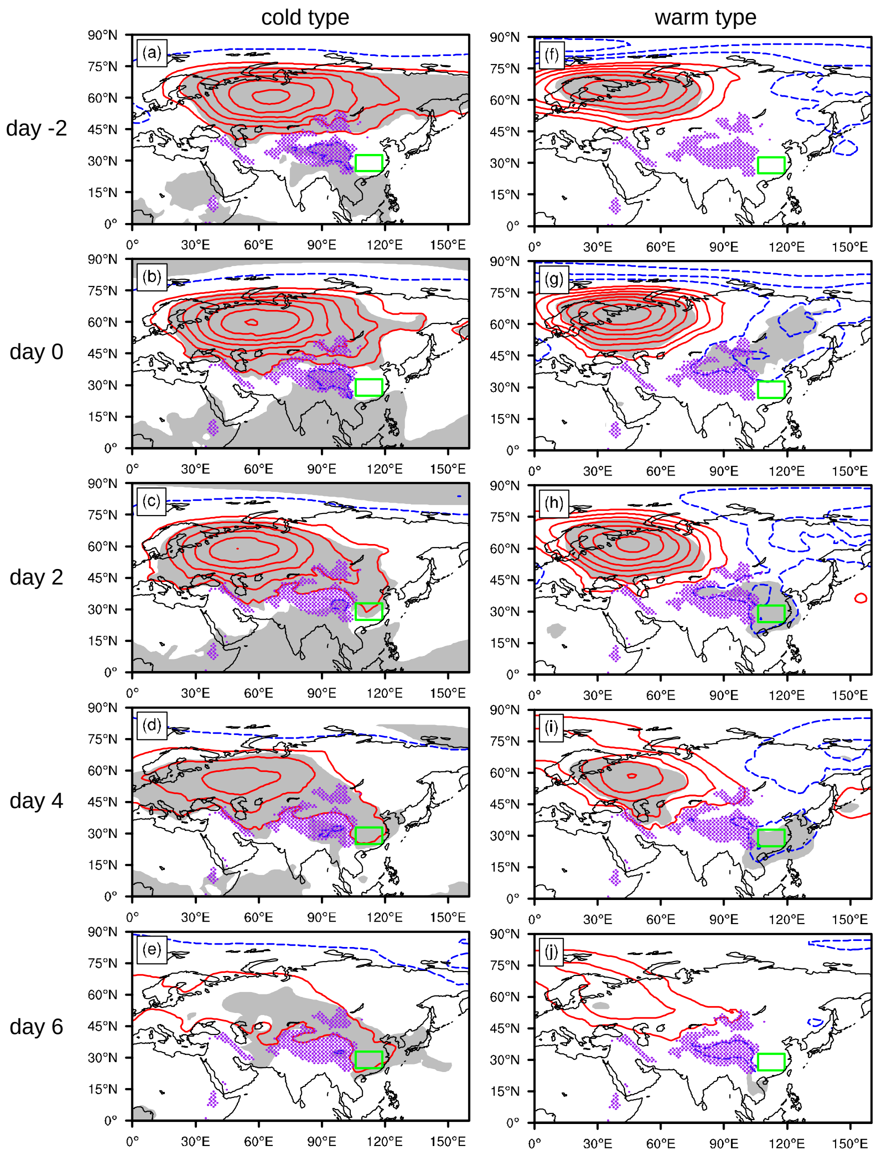

Figure 5 Composite evolutions of the SLP anomalies (hPa) associated with the 54 cold-type ESBs (left column) and the 24 warm-type ESBs (right column). Contours are drawn for ±3, ±6, …… hPa. Red solid lines and blue dashed lines represent positive and negative SLP anomalies, respectively. The gray shading denotes significant SLP anomalies according to Student's *t* tests with false discovery rates controlled by p^*_{FDR} ≈1.1% and 0.2% for the cold-type ESBs and the warm-type ESBs, respectively, computed with α_{FDR} =0.05. The green rectangle indicates the Yangtze River region. Purple stippling indicates that the topographic height exceeds 1500 m.

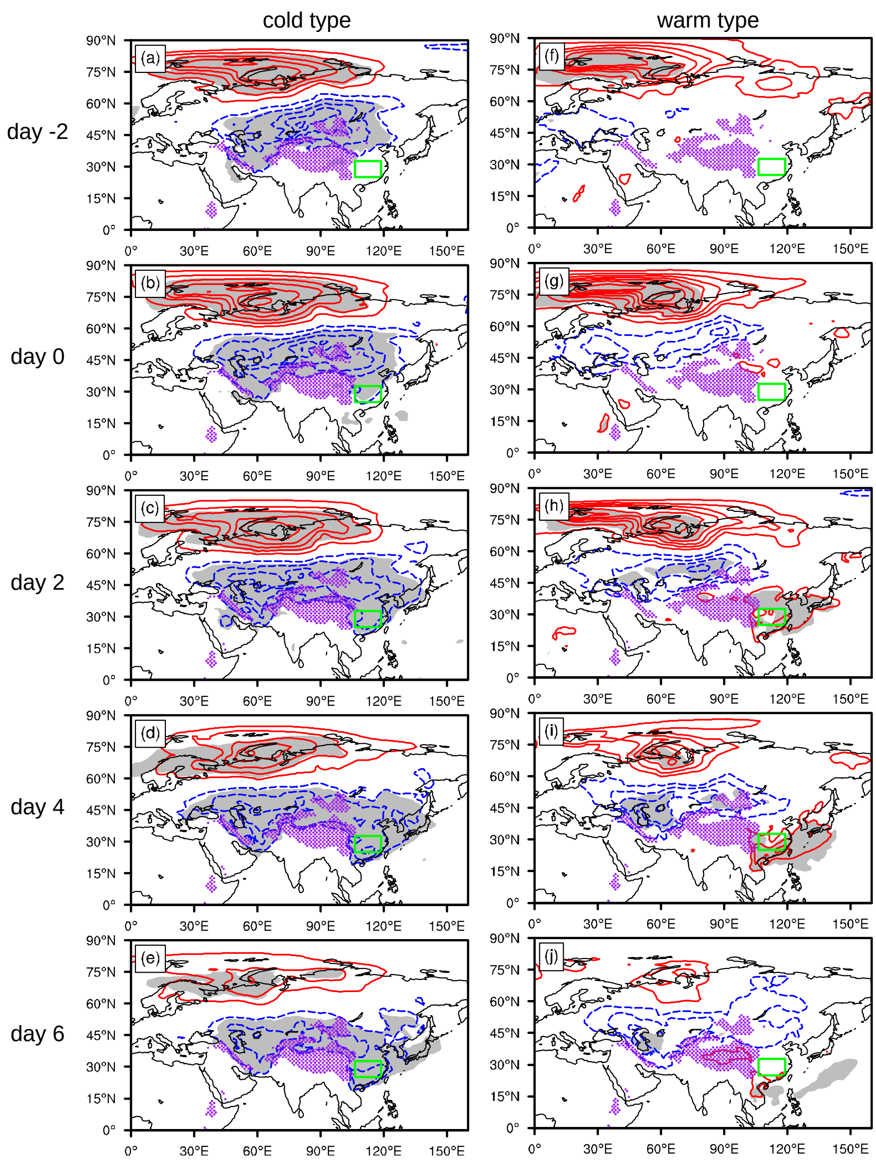

Figure 6 Same as Figure 5, but for the SAT anomalies (°C). Contours are drawn for ±1.5, ±3, ⋯⋯ °C. p^*_{FDR} is approximately 0.5% and 0.1% for the cold-type ESBs and the warm-type ESBs, respectively, computed with α_{FDR} =0.05.

Accepted for publication in *Monthly Weather Review*. DOI 10.1175/MWR-D-19-0152.1.

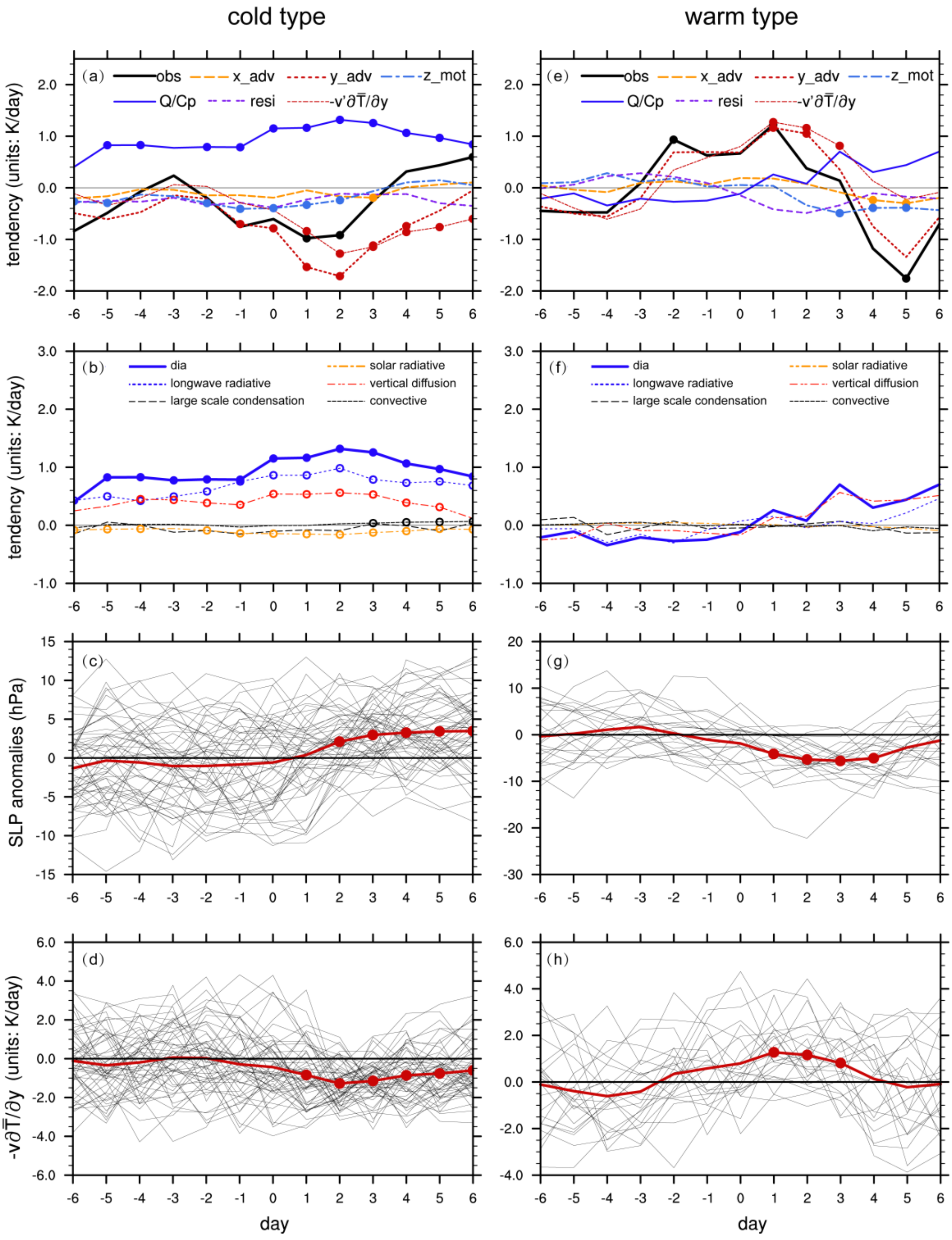

Figure 7 Statistics area-averaged over the Yangtze River region for (a-d) the 54 cold type ESBs and (e-h) the 24 warm type ESBs. (a), (e) Observed tendency of composite anomalous air temperature at 950 hPa and the contributions from every term of the right hand side of equation (3). (b), (f) Tendency of composite anomalous air temperature at 950 hPa due to the diabatic heating. (c), (g) Daily SLP anomalies (thin black lines) and the composite (thick red line). (d), (h) Meridional advection of the climatological mean by the anomalous meridional wind velocity $-v'\partial\overline{T}/\partial y$.

Accepted for publication in *Monthly Weather Review*. DOI 10.1175/MWR-D-19-0152.1.

Circles indicate the significant results at α_{FDR} =0.05 significant level.

Accepted for publication in *Monthly Weather Review*. DOI 10.1175/MWR-D-19-0152.1.

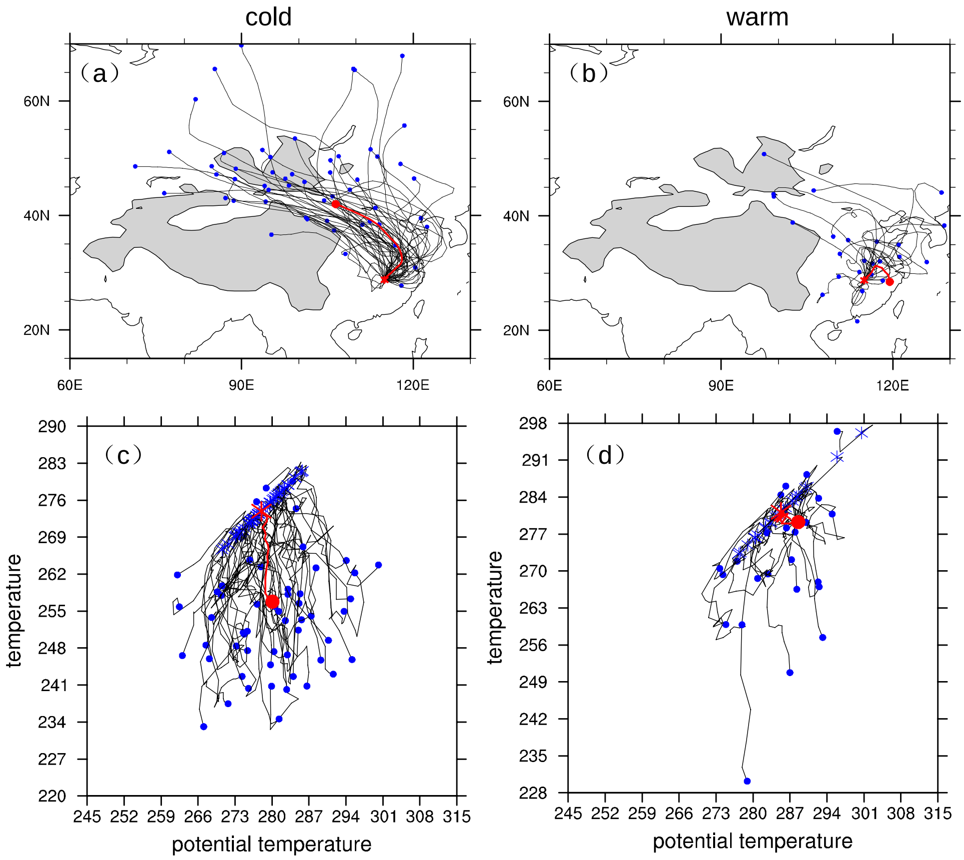

Figure 8 (a) Five-day backward trajectories of air parcels from the reference grid point [115ºE, 28.75ºN] at 950 hPa for the 54 cold-type ESBs starting from day 4. (c) The evolution of the temperature and potential temperature values for the trajectories shown in (a). The thick red lines in (a) and (c) are the results derived from the composite 54 cold-type ESBs. (b) and (d) Same as (a) and (c), respectively, but for the 24 warm-type ESBs. The red asterisks in (c) and (d) indicate the reference point at day 4, while the blue circles indicate the origin.

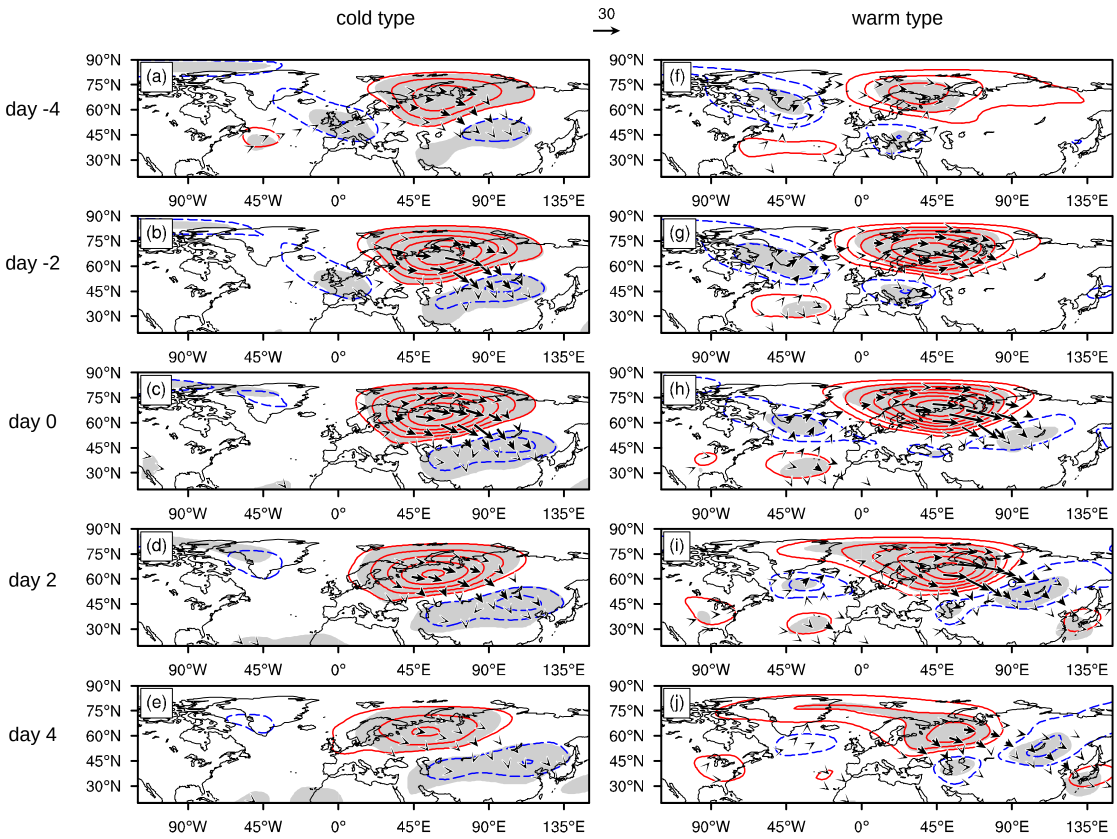

Figure 9 Same as Figure 5, but for the geopotential height anomalies at 300 hPa (contours, gpdm) and the associated wave activity flux (arrows, m^2/s^2). Contours are drawn for ± 5, ± 10, …… gpdm. The wave activity flux scale is plotted just above the top of (a). Wave activity fluxes with magnitudes of less than 4 m^2/s^2 are omitted. p^*_{FDR} is approximately 1.0% and 0.4% for the cold-type ESBs and the warm-type ESBs, respectively, computed with α_{FDR} =0.05.

Accepted for publication in *Monthly Weather Review*. DOI 10.1175/MWR-D-19-0152.1.

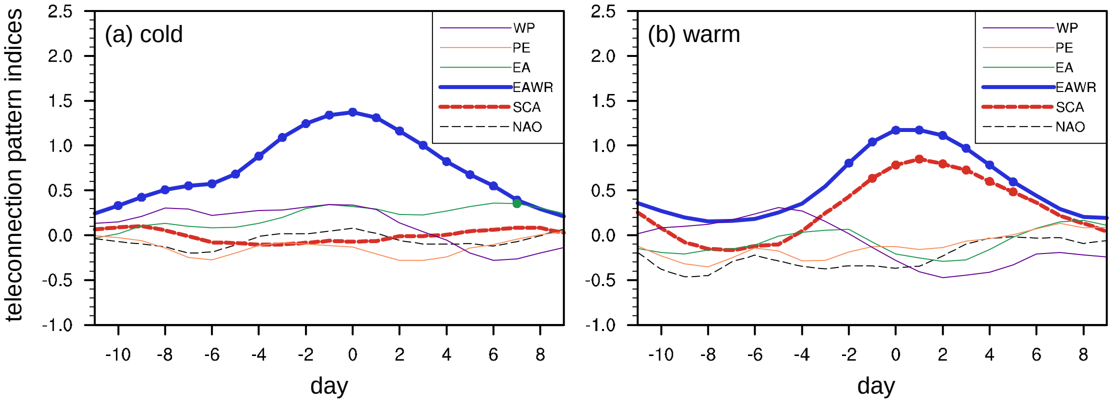

Figure 10 Composite indices of six teleconnection patterns during the evolution of (a) cold-type ESBs and (b) warm-type ESBs. “NAO” represents the Northern Atlantic Oscillation, “SCA” the Scandinavian pattern, “EAWR” the East Atlantic/West Russia pattern, “EA” the East Atlantic pattern, “PE” the polar/Eurasia pattern and “WP” the West Pacific pattern. Filled circles indicate the composite indices that are significant with α_{FDR} =0.05.

Accepted for publication in *Monthly Weather Review*. DOI 10.1175/MWR-D-19-0152.1.